Smart Mater. Struct. **31** (2022) 015018 (15pp) https://doi.org/10.1088/1361-665X/ac383d

Characterization of energy dissipative cushions made of Ni–Ti shape memory alloy

Ahmet Güllü[1,2,*], Josiah Owusu Danquah[3] and Savaş Dilibal[4]

[1] Department of Civil Engineering, Istanbul Gedik University, 34876 Istanbul, Turkey
[2] Department of Civil, Structural and Environmental Engineering, University at Buffalo, New York, United States of America
[3] Department of Civil and Environmental Engineering, Cleveland State University, Cleveland, OH, United States of America
[4] Department of Mechatronic Engineering, Istanbul Gedik University, 34876 Istanbul, Turkey

E-mail: ahmet.gullu@gedik.edu.tr

Received 1 August 2021, revised 12 October 2021
Accepted for publication 10 November 2021
Published 25 November 2021

Abstract
Earthquake-resistant design of structures requires dissipating seismic energy by deformations of structural members or additional fuse elements. Owing to its easy-to-produce, plug-and-play, high equivalent damping ratio, and large displacement capacity characteristics, energy dissipative steel cushions (SCs) were found to be an efficient candidate for this purpose. However, similar to other conventional metallic dampers, residual displacement after a strong shaking is the most notable drawback of the SCs. In this work, cushions produced from Ni–Ti shape memory alloy (SMA) are evaluated numerically by experimentally verified finite element models to assess their impact on the performance of earthquake-resistant structures. Furthermore, a reinforced concrete testing frame is retrofitted with energy dissipative steel and Ni–Ti cushions. Performance of the frames (e.g. dissipated energy by the cushions, hysteretic energy to input energy ratio, maximum drift, and residual drift) with different types of cushions are evaluated by nonlinear response history analyses. The numerical results showed that the SCs are effective to reduce peak responses, while Ni–Ti cushions are more favorable to reduce residual drifts and deformations. Hence, a hybrid system, employing the steel and SMA cushions together, is proposed to reach optimal seismic performance.

Keywords: shape memory alloys, energy dissipator, metallic damper, steel cushion, hysteretic response, nonlinear response history analyses

(Some figures may appear in color only in the online journal)

1. Introduction

Using energy dissipative fuse elements is a common way to enhance the seismic performance of structures in earthquake-prone areas. Interstory and/or roof drifts, accelerations as well as story shear forces can be reduced significantly by the fuses [1–3]. Many types of energy dissipative fuses, using distinct dissipation mechanisms, e.g. friction of metals [4], metallurgical properties of lead [5–7], yielding of metals [8], the viscosity of liquids [9], have been developed in the literature and applied to bridges [8], and high rise buildings [10].

Initially, the energy dissipative steel cushion (SC), a kind of metallic yielding damper, was developed as a connector to link reinforced concrete cladding panels to the main building [11–15]. In recent times, SC has also been utilized to retrofit frame-type structures [16–18].

The efficiency of SC was demonstrated in experimental and numerical manners under different loading conditions

* Author to whom any correspondence should be addressed.

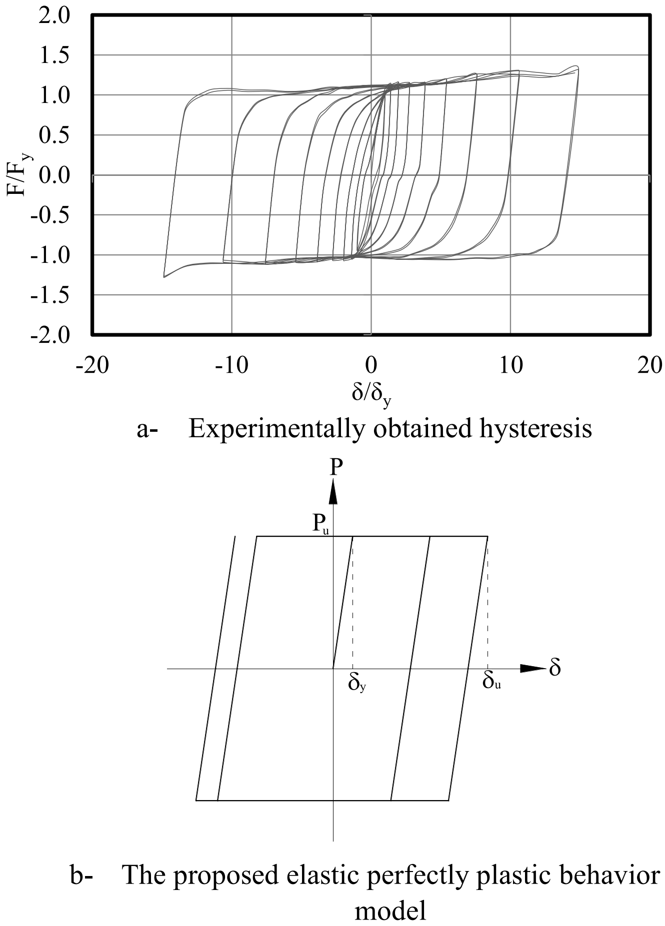

Figure 1. Hysteretic behavior of SCs.

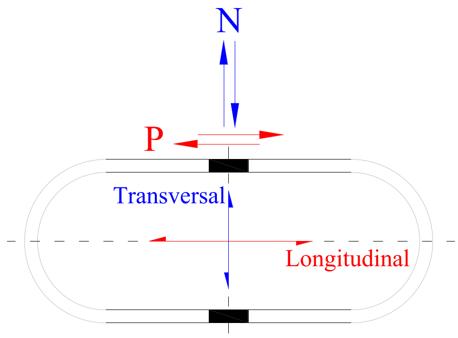

Figure 2. Loading type and directions for SC.

[12, 15, 19–21]. The experiments performed on SC [15, 16] resulted in almost rectangular hysteretic behavior, as demonstrated in figure 1(a). Hence, an elastic perfectly plastic model such as the one shown in figure 1(b) was proposed to simulate the hysteretic behavior of SC [15, 20]. The critical points of the model (yielding displacement, ultimate displacement, and yielding force) can also be calculated by closed-form equations [15, 20]. The experiments revealed that SC has a great displacement capacity which produces a displacement ductility up to 15.

Based on the performed studies, SCs were found to be more effective in the longitudinal (P) direction [19–21], see figure 2. The equivalent damping ratio of SC was found to be 50% in the longitudinal direction and only 18% in the transversal direction. Additionally, the displacement capacity of SC was larger in the longitudinal direction.

Besides its utmost benefits, residual displacement is the main drawback for SCs similar to other metallic dampers benefitting from the characteristics of steel. To supply self-centering property to the fuses, post-tensioned cables [22, 23] or shape memory alloys (SMAs) are generally preferred [24, 25].

SMA are used in several engineering fields, including aerospace, biomedical, and automotive, due to their lightweight, high fatigue strength, vibration absorption, and corrosion resistance properties. There are experimental and numerical studies in the literature that emphasizes the use of SMAs in reinforced concrete systems [26], passive and semi-active SMA dampers [27, 28], SMA based bracing systems [24, 29], bolted connections [30, 31], and vibration isolation system [32]. Recent studies unveiled that SMAs are significant candidates for vibration damping devices under dynamic loads [33, 34]. They can absorb the induced external loading energy via their unique superelastic behavior [35, 36].

The rationale of the present study is to investigate the effect of replacing the base material of an energy dissipative cushion (steel) with Ni–Ti SMA to enhance its post-earthquake behavior and self-centering characteristics. Finite element analyses of cushions produced from a SMA (SmaC) are performed initially. The resultant hysteretic behavior of SmaC is modeled as link elements to retrofit a testing frame. The contribution of SmaC to the overall seismic performance of the frame and its self-centering capacity is evaluated through nonlinear response history analyses.

2. Ni–Ti SMAs in energy dissipative systems

Metallic dampers benefitting from the characteristics of steel generally suffer from residual displacements after strong shakings. Therefore, different SMAs (e.g. nickel–titanium) were employed to supply self-centering.

Nickel–titanium (Ni–Ti) SMAs exhibit two significant properties through solid-to-solid reversible phase transformation [37]. The formation of the martensitic crystallographic structure from the austenitic phase occurs through stress-induced or thermal-induced martensitic transformations [38]. The thermal-induced martensitic transformation occurs through cooling; however, the stress-induced martensitic transformation forms under mechanical loading conditions. The reverse phase transformation occurs through unloading or heating. On the macro-scale, the reversible stress-induced martensitic transformation is referred to as the superelastic response of the Ni–Ti SMA while thermal-induced martensitic transformations are referred to as the shape memory effect. The thermal and mechanical loading can be used to stabilize the response of the SMAs [39, 40].

Ni–Ti SMAs are widely used in the field of dissipative energy systems by incorporating their superelastic property.

They show a reversible superelastic behavior up to 8% strain in experimental studies performed above the austenite finish temperature [41]. Their reversible solid-state phase transformation behavior makes them possible to use as passive energy absorption components. Their hysteretic damping capability has accelerated the use of Ni–Ti SMAs in earthquake engineering studies [42].

Bruno and Valente [43] have proven that SMA-based devices damped seismic vibration more than rubber insulators. Shape memory bearings are used in frame structures for energy distribution. During the loading, the wire tensioners made of SMAs dissipate energy by stress-induced martensite transformation or martensite reorientation [43]. Baratta and Corbi [44] reported that tendons produced from SMAs provide smaller residual strain and have excellent energy absorption ability [44]. DesRoches *et al* [45] reported that SMA restraints are more effective than steel cable limiters in bridge piers. Thanks to its high elastic strain range, SMA-based devices can undergo high deformation without losing their elasticity. Besides, owing to its superelastic behavior, SMAs provide energy distribution as a connecting element in corner joints [45].

Shi *et al* [46] generated probabilistic seismic demand models and fragility curves of steel frames with SMA bracing units exposed to mainshock—aftershock sequences. The bracing system was containing SMA cables in addition to the inner and outer steel parts. A previous nonlinear response history analysis indicated that the residual inter-story drift ratios of the frames were considerably reduced by SMA bracing. Cao *et al* [47] suggested a multi-level lead rubber bearing isolation system equipped with SMA wires to increase isolation efficiency and to limit excessive bearing displacement under earthquakes. Their proposed isolation system was found to be capable of limiting the bridge displacement to avoid pounding and girder unseating under earthquakes. Cao and Ozbulut [48] developed an SMA-based restrainer to limit relative displacements of adjacent spans of simply supported bridges. The restrainer consisted of a superelastic SMA bar, a steel tube, and a filler grout. The experimental study showed that the proposed restrainer exhibits a stable energy dissipator with self-centering capability. Zhang *et al* [49] amplified the SMA deformation using different inerter mechanisms to improve its energy dissipation capacity and vibration mitigation. It was found that the SMA-spring-paralleled inerter system enhances damping characteristics and requires lesser SMA material.

In terms of the manufacturing methodologies, subtractive or formative manufacturing processes can be used to fabricate the SMA cushions. However, in recent years hybrid or additive manufacturing technologies have been utilized for manufacturing SMA-based components in different systems [50, 51]. The reduction in the processing time and the ability to create complex geometry are the critical benefits of additive manufacturing technology. Additionally, structural stability is a vital process for Ni–Ti-based *SMA* components. The heat treatment strategy and hysteretic mechanical response of large size superelastic SMA have been examined experimentally for seismic application [52].

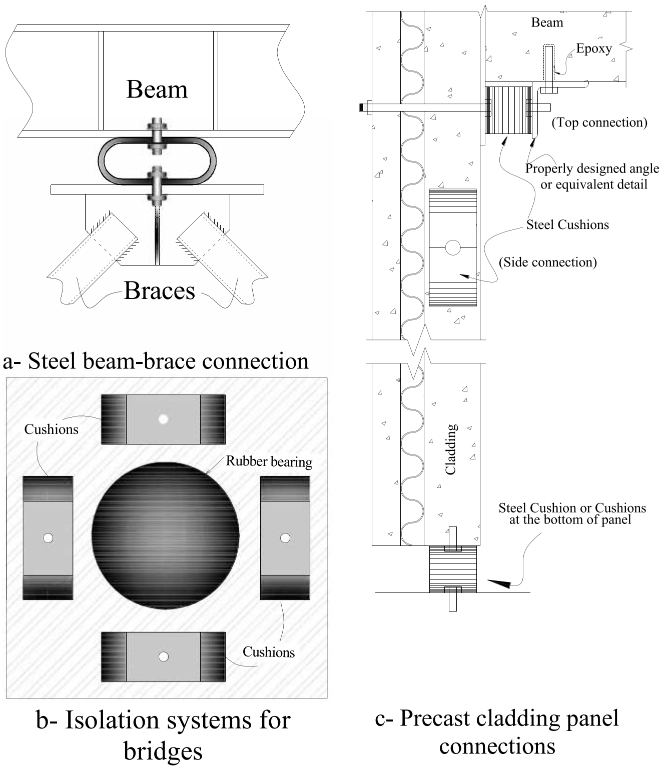

Figure 3. Possible application scenarios of the cushions.

3. Energy dissipative cushions produced from SMAs

Energy dissipative cushions can be utilized to enhance the seismic performance of structures with proper connections, see figure 3. Especially, they may limit the displacement demands of seismically isolated bridges and avoid pounding and/or girder unseating. Since the connections of the cushions are quite simple, they can be easily changed after an earthquake has occurred.

The numerical simulations conducted in this study involved two main steps: (a) application of a general constitutive model [53, 54] to characterize the superelastic behavior of the selected Ni–Ti SMA, and (b) subsequent implementation of the material model as user material (UMAT) model in a commercial finite element code for the analyses of the SMA dissipative cushion (SmaC). The model is currently specialized to only suit Abaqus finite element (FE) software (Dassault Systèmes Simulia Corp, 2013) as a UMAT subroutine. This allows us to later study several different structural forms of the SMA, e.g. beam, axisymmetric shell elements, 2D plane stress/plane strain elements, etc, which are available in Abaqus software. The multi mechanism material model is centered on the phenomenological approach, and once parameterized can be directly implemented into the Abaqus software.

3.1. Summary description of SMA constitutive model

The fundamental equations underlining the utilized material model are briefly stated in table 1 (other details can be found in Saleeb *et al* [37, 53–56]). The current section of the paper

Table 1. Summary of the set of equations used in the model formulation.

Equation set 1: decomposition of stress and strain:

$$\varepsilon_{ij} = \varepsilon_{ij}^{e} + \varepsilon_{ij}^{I};\ \alpha_{ij} = \sum_{b=1}^{N} \alpha_{ij}^{(b)}$$

Equation set 2: specific functional forms for stored energy and dissipation potentials:

$$\Phi_R = \frac{1}{2}\sigma_{ij}E_{ijkl}^{-1}\sigma_{kl};\ \Phi_{IR} = \sigma_{ij}\varepsilon_{ij}^{I} + \sum_{b=1}^{N}\bar{H}_{(b)}$$

$$\Omega = \int \frac{\kappa^2 F^n}{2\mu}\mathrm{d}F$$

$$E_{ijkl} = \frac{vE}{(1+v)}\delta_{ij}\delta_{kl} + \frac{E}{2(1+v)}\left(\delta_{ik}\delta_{jl} + \delta_{il}\delta_{jk}\right).$$

Equation set 3: evolutionary laws:

$$\dot{\varepsilon}_{ij} - \dot{\varepsilon}_{ij}^{I} = \frac{d}{dt}\left(\frac{\partial \Phi_R}{\partial \sigma_{ij}}\right) = E_{ijkl}^{-1}\dot{\sigma}_{kl};\ \dot{\varepsilon}_{ij}^{I} = \frac{\partial \Omega}{\partial \sigma_{ij}}$$

$$\dot{\alpha}_{kl}^{(b)} = \left[\frac{\partial^2 \Phi_{IR}}{\partial \alpha_{ij}^{(b)}\partial \alpha_{kl}^{(b)}}\right]^{-1}\dot{\gamma}_{ij}^{(b)};\ \dot{\gamma}_{ij}^{(b)} = -\frac{\partial \Omega}{\partial \alpha_{ij}^{(b)}}.$$

Equation set 4: transformation and hardening functions:

$$F = \frac{1}{\kappa^2}\left[\frac{1}{2\rho^2}\left(\sigma_{ij} - \alpha_{ij}\right)M_{ijkl}\left(\sigma_{kl} - \alpha_{kl}\right)\right]$$

$$\underset{(b)}{\bar{H}} = \begin{cases} \kappa_{(b)}^2 \int \dfrac{1}{\bar{h}\left(g^{(b)}\right)}\mathrm{d}G^{(b)}, \text{for } b = 1,2,3; \\ \kappa_{(b)}^2 \int \dfrac{1}{h\left(G^{(b)}\right)}\mathrm{d}G^{(b)}, \text{for } b \geqslant 4; \end{cases}$$

$$\bar{h}\left(g^{(b)}\right) = \begin{cases} \dfrac{\rho_{(b)}\kappa_{(b)}H_{(b)}\left(\sqrt{g^{(b)}}\right)^{\left(\beta_{(b)}-1\right)}}{\kappa_{(b)} + H_{(b)}\left(\sqrt{g^{(b)}}\right)^{\beta_{(b)}}}, & \text{for } b = 1,2, \\ \rho_{(b)}H_{(b)}\left[1 + \left(\dfrac{\sqrt{g^{(b)}}}{\kappa_{(b)}/H_{(b)}}\right)^{\beta_{(b)}}\right], & \text{for } b = 3, \end{cases}$$

$$h\left(G^{(b)}\right) = H_{(b)}\left[1 - \left(\frac{\sqrt{G^{(b)}}}{\rho_{(b)}}\right)^{\beta_{(b)}}\hat{h}(L)\right], \text{ for } b \geqslant 4;$$

where,

$$G^{(b)}\left(\alpha_{ij}^{(b)}\right) = \frac{1}{2\kappa_{(b)}^2}\left(\alpha_{ij}^{(b)}M_{ijkl}\alpha_{kl}^{(b)}\right)$$

$$g^{(b)} = \gamma_{ij}^{(b)}M_{ijkl}\gamma_{kl}^{(b)}$$

$$\rho = \frac{1 + c\sqrt{d}}{1 + c\sqrt{d + k_3}} \text{ and } \rho_{(b)} = 1$$

focused on the direct implementation of the developed model to simulate the cyclic behavior of the SmaC. In principle, the model uses multiple inelastic mechanisms (representing energy dissipation and energy storage) and state variables to characterize the deformation processes associated with SMAs. For energy storage, Gibb's complimentary free energy, Φ is used with Φ_R and Φ_{IR} representing the elastic and inelastic parts, respectively. Besides, the potential energy function, Ω is used for inelastic energy dissipation.

The state variables in the model are grouped into external and internal (hidden) variables. The scalar temperature, T, the 2nd-order stress tensor, σ_{ij}, and its corresponding conjugate strain tensor, ε_{ij}, constitute the external state variables. These variables serve as the controllable input-output responses of the material. Here, we take temperature as a controllable variable, thus we neglect the effect of latent heat generation/absorption. The external variables σ_{ij}, and ε_{ij} provide the needed mechanical control input and the corresponding measured output for a specific test procedure. As will be shown in subsequent sections, in a strain/displacement-controlled test, all the components of ε_{ij} are specified, whereas the components σ_{ij} constitute the measurable material response.

The hidden variables are the inelastic transformation strain tensor, ε_{ij}^{I}, the back stress, $\sigma_{ij}^{(b)}$, for kinematic hardening, and their conjugate strain-like variables, $\gamma_{ij}^{(b)}$ (where the superscript b is a counter denoting a specific inelastic mechanism). In its most recent form, only six mechanisms are activated in the model. Specific roles played by each of these mechanisms in capturing the internal microplasticity, dislocations, micro defects, occurring within a material during martensitic phase transformation from one crystal structure to the other have been explained in Owusu-Danquah *et al* [55].

From the above set of equations, a total of 25 parameters are typically needed if all the six mechanisms are activated in a material characterization procedure. These include seven constant parameters E, v, κ, μ, n, c, d, and 18-mechanism based parameters, i.e. six for $H_{(b)}$, six for $\beta_{(b)}$, and six for $\kappa_{(b)}$ (where the superscript b is a counter denoting a specific mechanism).

3.2. Model parameterization for superelastic Ni–Ti material

For the present task of characterizing the superelastic behavior of the SMA at a constant temperature (greater than the austenite finish, A_f), the Ni–Ti alloy is assumed to exhibit superelastic behavior at room temperature. Here, only two storage mechanisms, $b = 1$, 3, and two dissipative mechanisms, $b = 4$, 5 are activated; this reduces the total needed model parameters to 19. The numerical values for these parameters are stated in table 2 and were selected following the procedures suggested in [50, 51].

The main differences between the current framework model and other well-known Abaqus in-built models are that: (a) this UMAT model does not employ the concept of scalar phase (or volume) fractions of martensite variants as internal variables, (b) the inelastic strain tensor in the model is not decomposed into different parts, and (c) it is highly general to enable us to capture the superelastic, isobaric, isostrain, cyclic one-way,

Table 2. Model parameters of Ni–Ti.

Parameter	Unit			Value	
			Elastic constants		
E	GPa			45	
v	—			0.3	
			Inelastic constants		
No. of mechanisms	—			4	
n	—			5	
μ	MPa.s			10^5	
κ	MPa			20	
$\kappa_{(b)}$ $b = 1, 3, 4$, and 5	MPa	265	16.5	12.5	2
$\beta_{(b)}$ $b = 1, 3, 4$, and 5	—	1	5.5	1	1
$H_{(b)}$ $b = 1, 3, 4$, and 5	MPa	5×10^5	300	5×10^4	10^3
			Asymmetry constants		
c	—		1.0		
d	—		1.5		

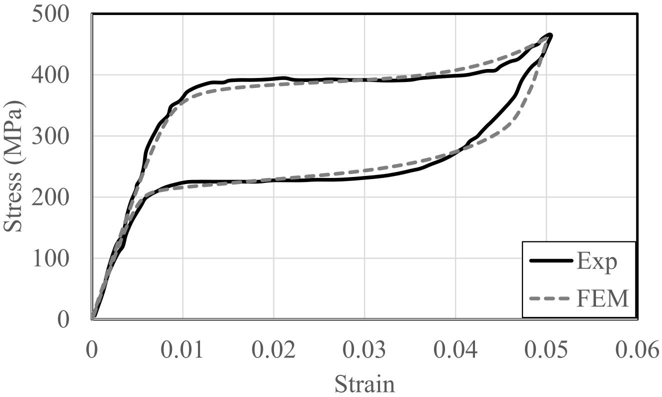

Figure 4. Model vs experiment stress–strain response of superelastic Ni–Ti under the tensile strain of 0.05.

two-way shape memory responses of virgin and trained SMAs using the same set of equations and/or parameters [37, 54].

Figure 4 shows the model-predicted (labeled as FEM) and the experimental (Exp) [57] tensile stress vs strain response of the Ni–Ti material at room temperature. In this material point test, the sample was subjected to a uniaxial tensile strain of 5% and then unloaded from this strain magnitude to zero stress. It is seen that the superelastic material can recover almost all of the induced deformation once it is unloaded from the 5% strain. Moreover, there is a good correlation between the experiment and model results. The area within the hysteresis loop characterizes the dissipated energy per unit volume of the material. Figure 5 shows the different hysteretic responses exhibited by the material when subjected to varying strain paths, all indicating the high energy dissipative properties of the Ni–Ti SMA.

In applications where the alloy can experience stress reversals, it is important to also model the differences in material responses under compression (to ascertain the ATC effects). Lacking the compression component of the experimental plot, only the model-predicted responses are shown in figure 6. It is seen that under the same targeted strain of 0.05, the stresses obtained in the tensile case are slightly lesser than the case of compression, i.e. the tensile stress of 450 MPa and compressive stress of 500 MPa. Recent experimental work by Qiu *et al* [58] also showed the asymmetry tension-compression behavior of SMA bars tested under cycles. The tension–compression asymmetry is attributed to the crystallographic asymmetry of the martensitic phase transformation. The model parameters c, and d are used to account for the intensity of asymmetry in stress–strain behaviors when the SMA is loaded in tension versus compression versus shear (i.e. ATC effects). The effect of the c and d in characterizing some of the experimentally-observed ATC can be found in Saleeb *et al* [53].

3.3. Numerical simulation of the SmaC

Using the parameterized model as a UMAT in Abaqus finite element code, the SmaC device was modeled and analyzed under nonlinear static conditions, using the unconditionally stable, fully-implicit, backward Euler difference integration scheme. The SmaC (shown in figure 7) was placed between two rigid walls (taken to be materials of relatively high elastic modulus in comparison to that of the Ni–Ti). One of the walls was fixed against translation and rotation in x-, y-, and z-axes, while the other end was made to transmit the cyclic longitudinal displacements to the SmaC. For the sake of simplicity, the walls were coupled to reference points through the kinematic coupling property.

Interactions between the walls and the SmaC, as well as between the SmaC and the bolts, were defined through the surface to surface contact. In the contact interaction property, the 'hard contact' and 'penalty' were selected for the normal and tangential behaviors, respectively.

To decrease computational costs while increasing the accuracy of FEM, 2D four-noded quadrilateral shell elements (S4R) were employed in the models. The shell thicknesses were taken to be 8 mm for both the walls and the SmaC. From a preliminary mesh convergence study, 160 elements were considered adequate for the cushion. The meshed configuration of the SmaC with the walls is illustrated in figure 8.

Two main cyclic loading protocols, labeled as case A and case B were considered under the same boundary, geometric conditions of the SmaC to study its performance characteristics under varying load-displacement patterns, figure 9. In these simulations, the maximum shear angle γ (defined in figure 10) was 0.75 rad [59]. Specifically, the displacement protocol given as case A is significantly important for the energy-based seismic design to demonstrate that deformations may increase after ultimate cycles, hence, duration-related cumulative damage must be considered, Güllü *et al* [60].

The force vs displacement history of the identical SmaC and SC under cases A and B are compared in figures 11(a) and (b), respectively. Unlike the case of the elastoplastic steel material, it is seen here that there is no residual displacement

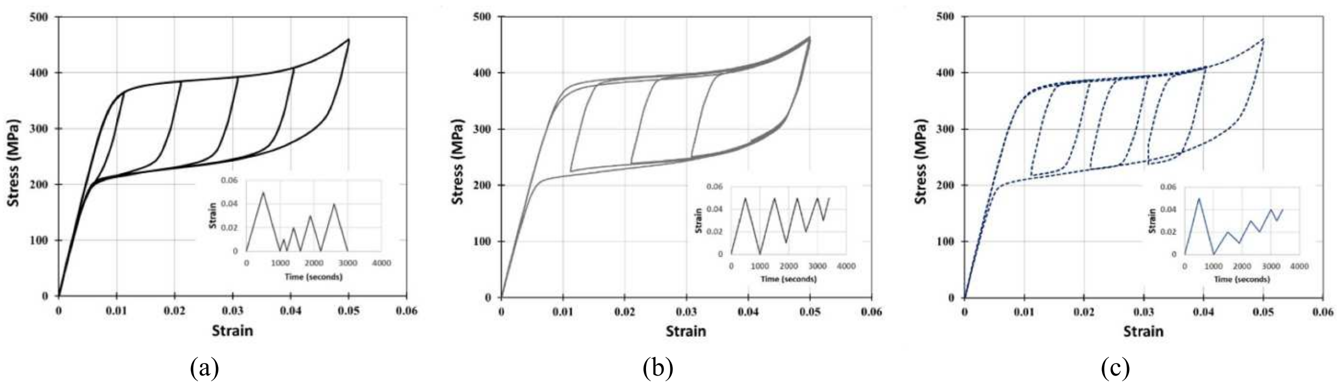

Figure 5. Model responses of the superelastic Ni–Ti under varying strain paths.

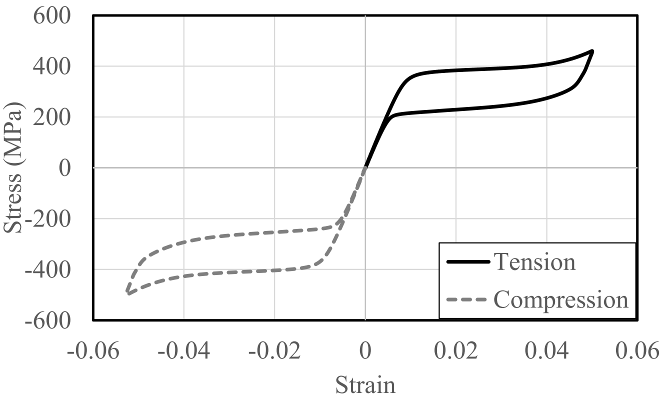

Figure 6. Model stress vs strain response of superelastic Ni–Ti under the tensile and compressive strain of ± 0.05 to demonstrate the effect of the ATC model parameters (c), (d).

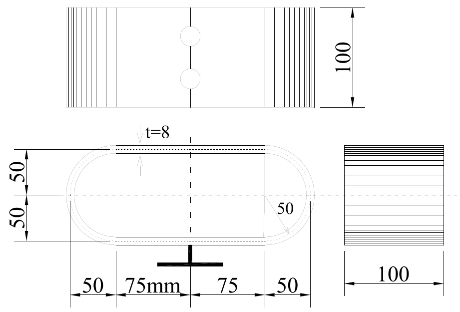

Figure 7. Geometric properties of the energy dissipative cushions (dimensions are in mm).

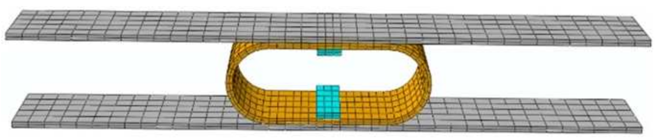

Figure 8. Meshing of FEM.

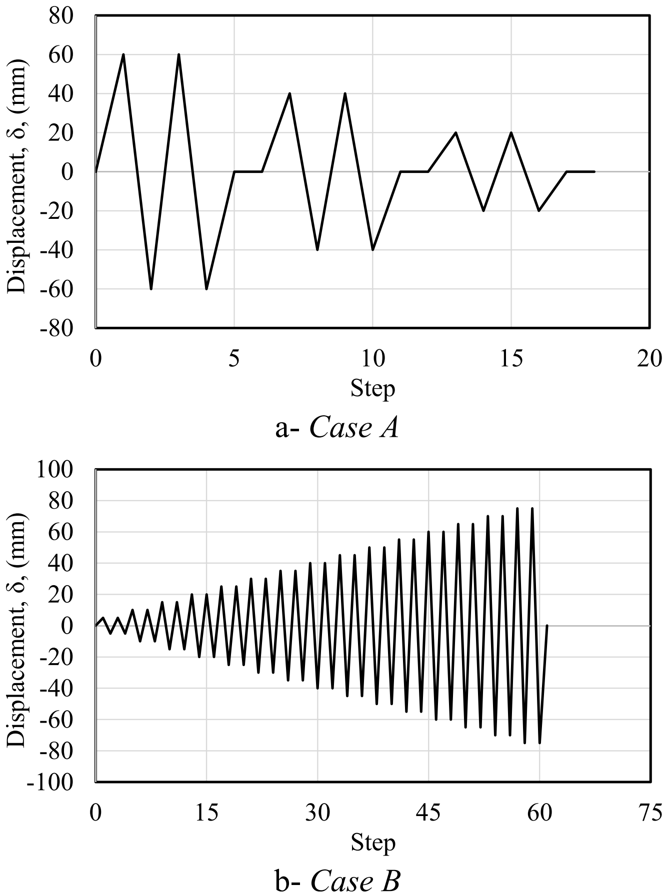

Figure 9. Imposed cyclic loadings to FEMs.

at the end of each cycle in the SmaC. Looking at the results for case A, there is an increase in the force from zero to a value of 28 kN at the end of the 1st cycle displacement of 60 mm. Upon unloading to zero displacement and reloading on the (opposing side), the force changed from zero to -30 kN (in the compression side). For case B, the maximum force obtained at the end of +75 mm displacement was 33.133 kN. It is obvious that between 40 and 75 mm displacement, there is no significant difference between the force measured. In particular, only a change of about 1.187 kN occurs in the tensile side and 0.391 kN on the compression side between ± 40 mm and ± 75 mm. This is related to the material point behavior in figure 5, where a significant portion of the stress–strain response is dominated by the middle (almost flat) plateau region signifying the state of the material dominated by

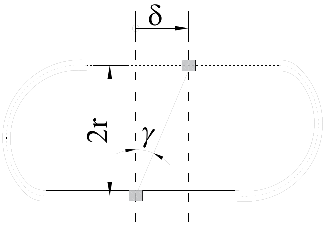

Figure 10. Definition of the shear angle γ.

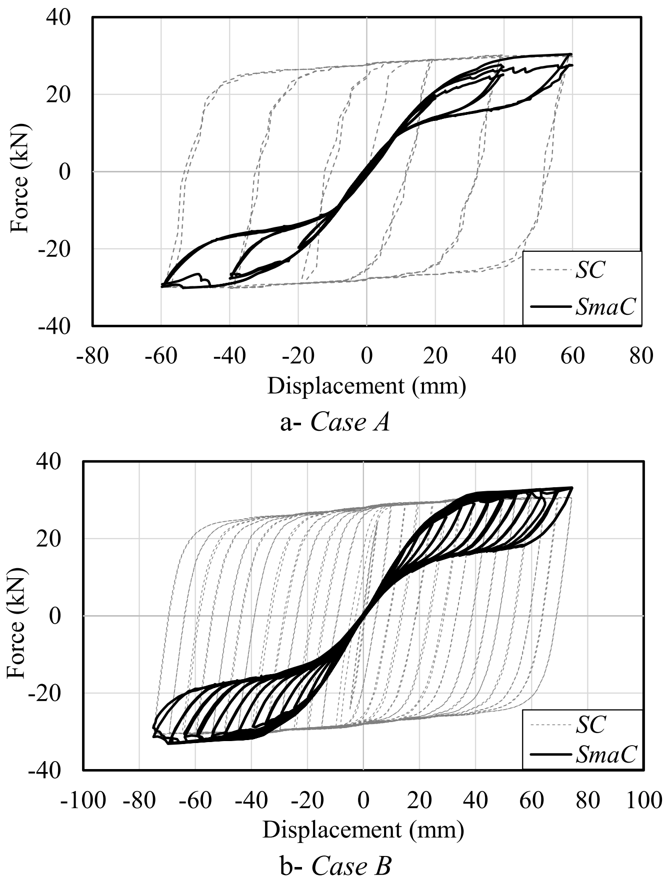

Figure 11. Comparison of force-displacement histories of energy dissipative cushions.

Table 3. Some characteristics of the dampers are derived from finite element analyses.

Parameter	Case A		Case B	
	SmaC	SC	SmaC	SC
Initial stiffness (kN mm^{-1})	1.083	5.385	1.087	5.284
Secant stiffness (kN mm^{-1})	0.508	0.503	0.446	0.412
Yielding force (kN)	20.153	24.658	20.223	24.053
Ultimate force (kN)	30.424	30.176	33.214	30.669
Damping ratio (%)	8.045	52.279	9.827	53.448
Residual disp (mm)	0.000	52.084	0.000	67.171

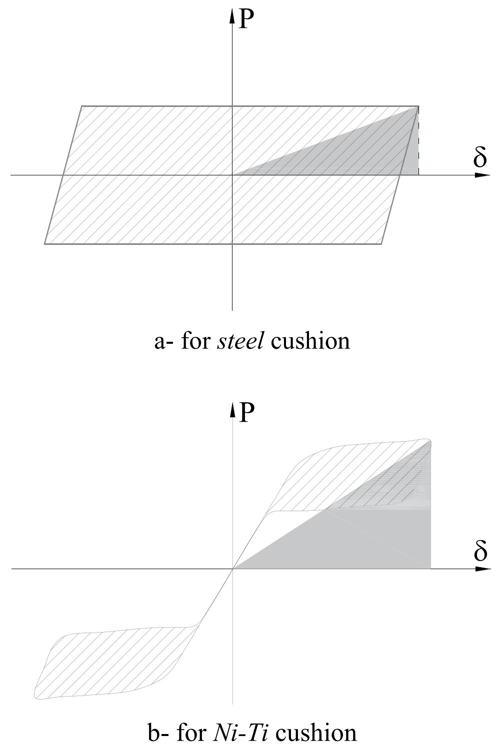

Figure 12. Determination of damping ratio for the dampers.

the reoriented/detwinned martensite variants (between strains of 0.012 and 0.046).

It is worth mentioning that in the characterization of the present model, we did not account for the effect of the geometry or post-processing treatment of the test coupons on the material response. Rather, it was assumed that the observed stress–strain responses in figure 4(a) reflected the final intrinsic material point behavior of the SmaC. Previous studies by Owusu-Danquah and Saleeb [56, 61] describes the application of the model to investigate the effect of geometry and heat treatment on the cyclic response of SMA actuators. Their work indicated that the functional performance of shape memory devices is highly influenced by the device geometry and heat treatment of the material.

General characteristics of the force-displacement histories of SmaC and SC are also compared in table 3. The initial stiffness of SmaC is considerably lower than SC. However, the secant stiffnesses of the dampers, that were calculated at the maximum displacement level, are similar between the two cushion types. It is found for both loading cases that the yielding forces of the SmaC and SC are about 20 and 24 kN, respectively. In loading case A, the ultimate forces of the dampers were similar. Since hardening is more evident for SMAs, the ultimate force of the SmaC is almost 10% higher than that of the SC. The foremost differences between the dampers were related to damping ratio and residual displacement. The residual displacements of the SmaC were nearly zero in the two loading cases, in contrast to that of the SC where a maximum residual displacement of 67.17 mm was evaluated. Consequently, the equivalent damping ratio of the SC is calculated to be ~53% while it is found to be 8%–10% for SmaC. The damping ratio (ξ) was calculated by using equation (1), where E_D and E_S are depicted in figure 12 with dashed and solid hatched areas, respectively [62, 63].

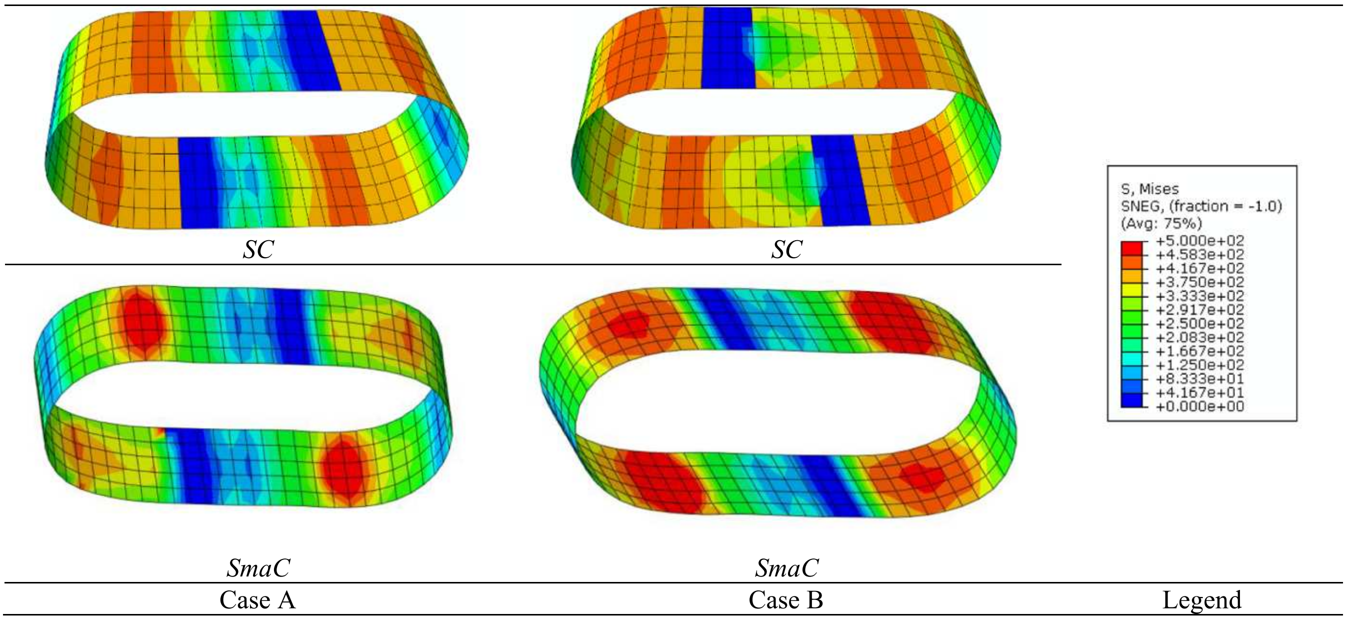

a) von Misses stress distribution on the cushions.

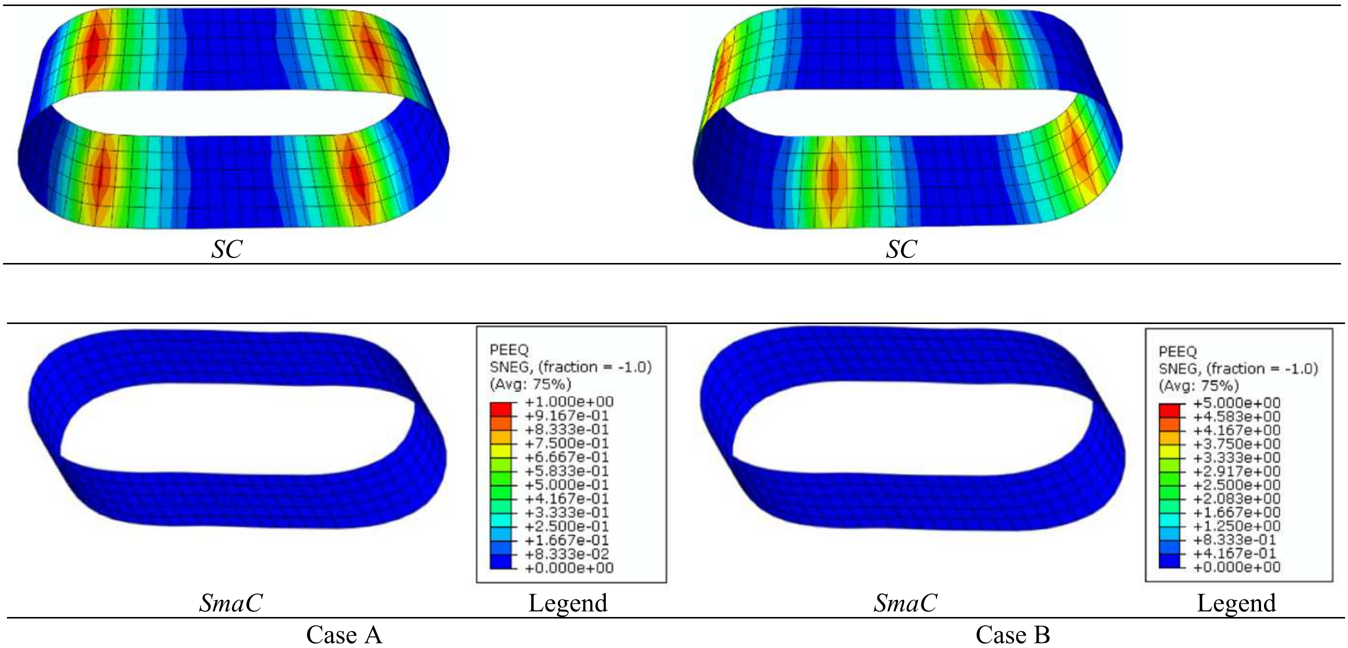

b) Equivalent plastic strain distribution on the cushions.

Figure 13. Obtained maximum stresses and plastic strains on the cushions.

$$\xi = \frac{1}{4\pi}\frac{E_D}{E_S}. \tag{1}$$

Stress and plastic strain distributions on the cushions are also compared in figures 13(a) and (b). While the ultimate stresses achieved on both cushions are comparable, the equivalent plastic strains are considerably lower for SmaC.

In all cycles, the forces read almost zero every time the applied displacement is brought to zero in both cases. Comparing figure 11 (of the SMA part) to the previous figure 4, one realizes that the tension-compression asymmetry (ATC) in Ni–Ti responses is less noticeable in the structural SmaC simulation when compared to the material point characterization. This is because the material in the structural form interacts with the geometry of the device, hence become subjected to non-homogeneous conditions which affect the 'true' material response. Notwithstanding, the presence of the SMA endues the damper with high recentering capability. The hardening nature of the SMA material attempted to limit the deformations that occur during the cyclic loading, while the superelastic, recentering feature tended to restore the structure to the original state.

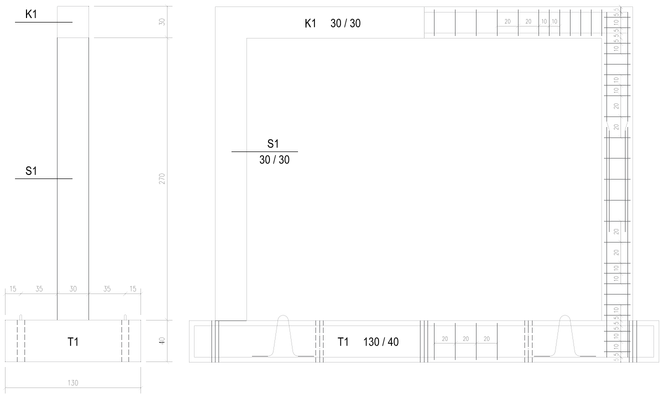

Figure 14. Bare testing frame.

4. Retrofitting of a testing frame with the dampers

Numerical models of an experimental testing frame are generated in this section to compare the effect of the distinct cushions for retrofitting purposes of the frame [64]. Here, the simulations were performed using SAP2000® FE software. The frame is representative of residential buildings in Turkey with a 4.0 m length and 3.0 m height, figure 14. The columns and beams have a 300 × 300 mm^2 cross-section. Columns have 8Ø16 longitudinal reinforcement. The beam has 3Ø14 longitudinal reinforcements at the top and bottom sections. All of the elements have Ø10/10–20 transversal reinforcement. The foundation of the frame has 400 mm thickness, 4500 mm length, and 1300 mm width.

The quasi-static bare frame experiment was performed by Safarli [65]. In their study, the 28 day compressive strength of the concrete was determined to be 33.7 MPa. The yielding and ultimate stresses of the rebar were also found to be 420 and 500 MPa, respectively.

In the numerical model, the nonlinear behaviors of the frame elements are defined by fiber hinges, whereas the hysteretic behaviors of the cushions are represented with link elements. The Bouc–Wen model is employed for SC [66], while multiple multilinear elastic and plastic links with a pivot hysteresis model are utilized to define the superelastic behavior of SmaC [67]. It is worth noting that the numerical modeling assumption for SMA was also employed by Cao *et al* [47].

A secondary frame, designed by using IPE220 steel profile, is also modeled to fix the cushions to the mainframe as described by Güllü [17] and Güllü *et al* [18]. The generated numerical model is depicted in figure 15.

The necessary parameters to define the link elements are tabulated in table 4. The post-yield stiffness ratio of the SC (stf ratio) can be neglected [16]. The β parameters of the pivot model are effective on the self-centering capability of SmaC. Taking the parameters β_1 and β_2 as zero results in ideal self-centering.

Similar to Cao *et al* [47], the force-displacement relation of SmaC is simplified for practical modeling (figure 16).

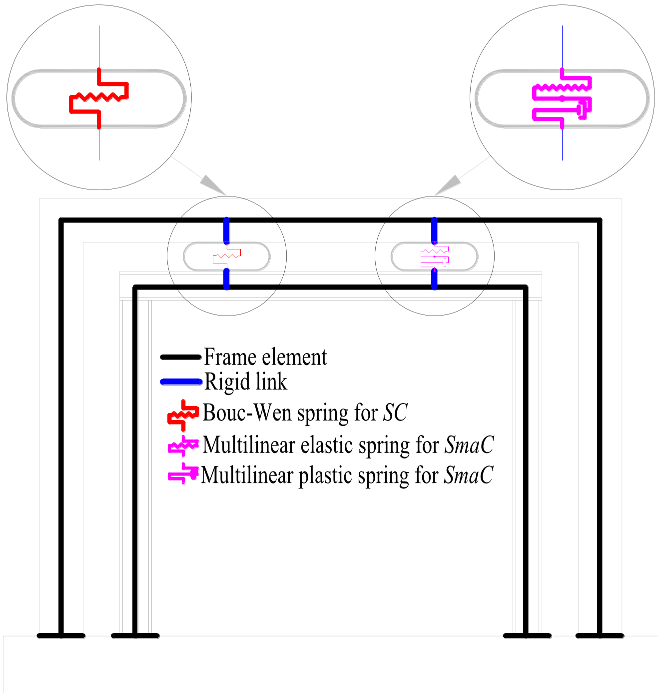

Figure 15. Numerical modeling strategy.

Table 4. Link element parameters.

Link	Property	Unit	Value
SC Bouc–Wen	Stiffness	kNm	4500
	Yield force	kN	34
	Stf ratio	—	0.001
	Yield exp	—	0.5
SmaC Pivot	$\alpha_1 = \alpha_2$	—	100 000
	$\beta_1 = \beta_2$	—	0
	η	—	1

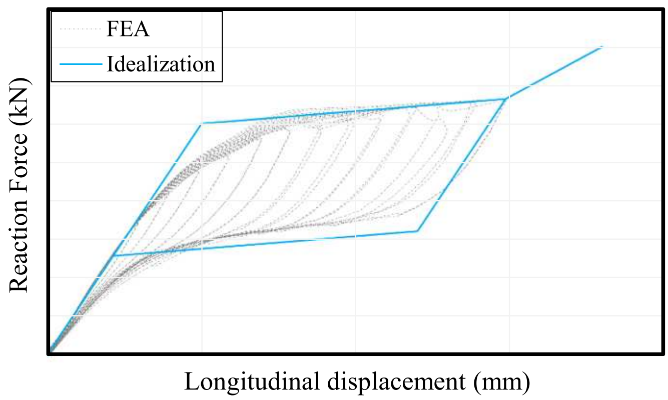

Figure 16. Simplified hysteretic behavior of the SmaC.

4.1. Verification of the numerical model for the bare frame

At the outset, the base model is verified through experimental results for further numerical analyses. In the quasi-static cyclic experiments, the loading pattern was created considering ACI-374 2R [68]. Accordingly, the displacement targets were

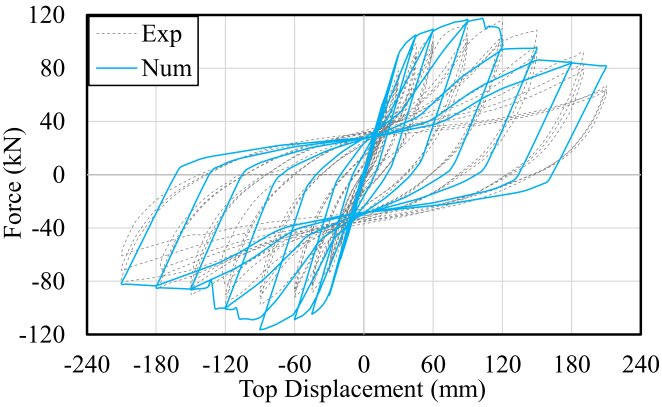

Figure 17. Comparison of force-displacement relations obtained experimentally and numerically. Reproduced with permission from [65].

achieved to be ±1, 3, 10, 20, 30, 45, 60, 90, 120, 150, 180 and 210 mm [68].

The numerical force-displacement relation (blue solid line) obtained for the bare frame is compared with the experimental one (gray dashed line) in figure 17.

Based on the comparison, it can be said that the numerical model satisfactorily captures the hysteretic behavior of the bare frame.

4.2. Response history analyses

The bare frame (BF) and the frames with two steel cushions (SF), two SMA cushions (SmaF), as well as a hybrid frame (HF), are exposed to several historical ground motion records obtained from the NGA database [69]. The hybrid frame includes one SC and one SmaC. Even though the axial force effect was neglected in the experiments, the axial force ratio of 20% is assumed in the analyses.

4.2.1. Record selection and scaling. Historical ground motion records caused by the strike-slip faulting mechanism are selected for the analyses. Additionally, the shear wave velocity of the upper 30 m of the soil (V_{s30}), where the ground motions were recorded, is restricted between 360 and 760 m s^{-1}. The characteristic properties of the records are given in table 5. In the table, RSN is the record sequence number, Mag is the earthquake magnitude, EQ infers to the location where the earthquake occurred, R_{rup} is the rupture to distance.

The selected records were scaled in the period range of 0.05–2.00 s by the procedure proposed by Al Atik and Abrahamson [70]. The target spectrum was constructed for Istanbul based on the parameters given by the Turkish Building Earthquake Code [71]. Time histories of the matched records are illustrated in figure 18. Peak ground accelerations of the matched records vary between ±0.5 g. Additionally, the 5% damped target spectrum and the acceleration spectra (SA) of matched records are shown in figure 19.

Table 5. Some properties of the selected records.

RSN	EQ	Mag	R_{rup} (km)	V_{s30} (m s^{-1})
164	Imperial valley	6.53	15.19	472
265	Victoria, Mexico	6.33	14.37	472
448	Morgan Hill	6.19	3.26	489
864	Landers	7.28	11.03	380
901	Big Bear	6.46	8.30	430
1111	Kobe, Japan	6.90	7.08	609
1617	Duzce, Turkey	7.14	3.93	454

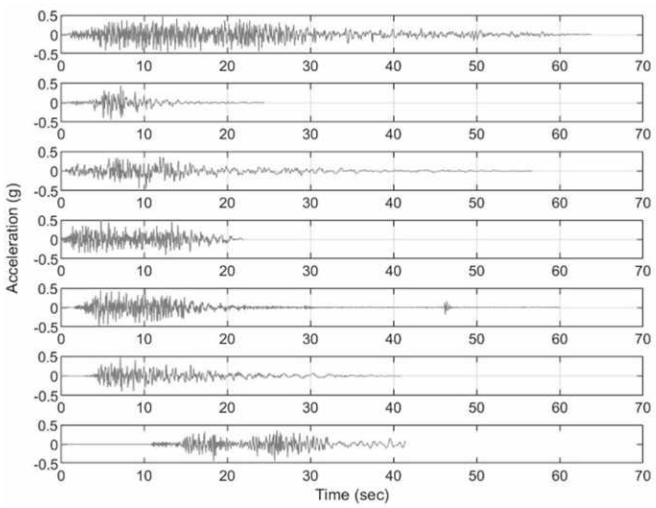

Figure 18. Time histories of the matched records.

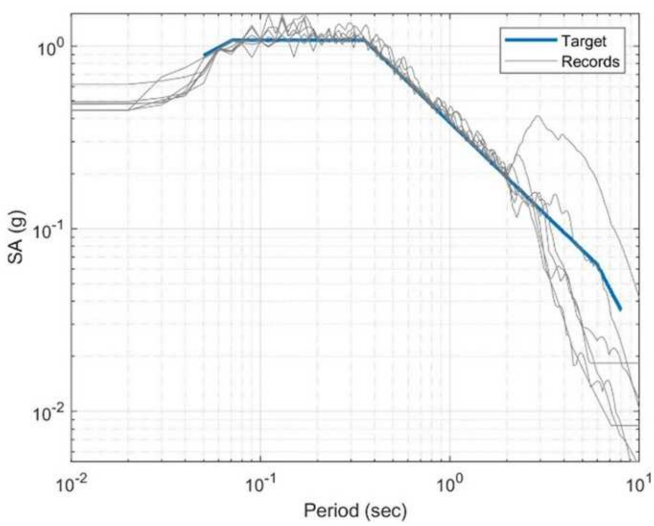

Figure 19. Acceleration spectra of the scaled records and the target spectrum.

4.2.2. Analyses results. The numerical models of the BF, SF, SmaF, and HF are exposed to the selected and scaled ground motions. At the outset, seismic input energy imparted to the frames and distribution of its subcomponents is evaluated. The energy balance equation in the time domain proposed by Akiyama [72] was used, see equation (2). In the

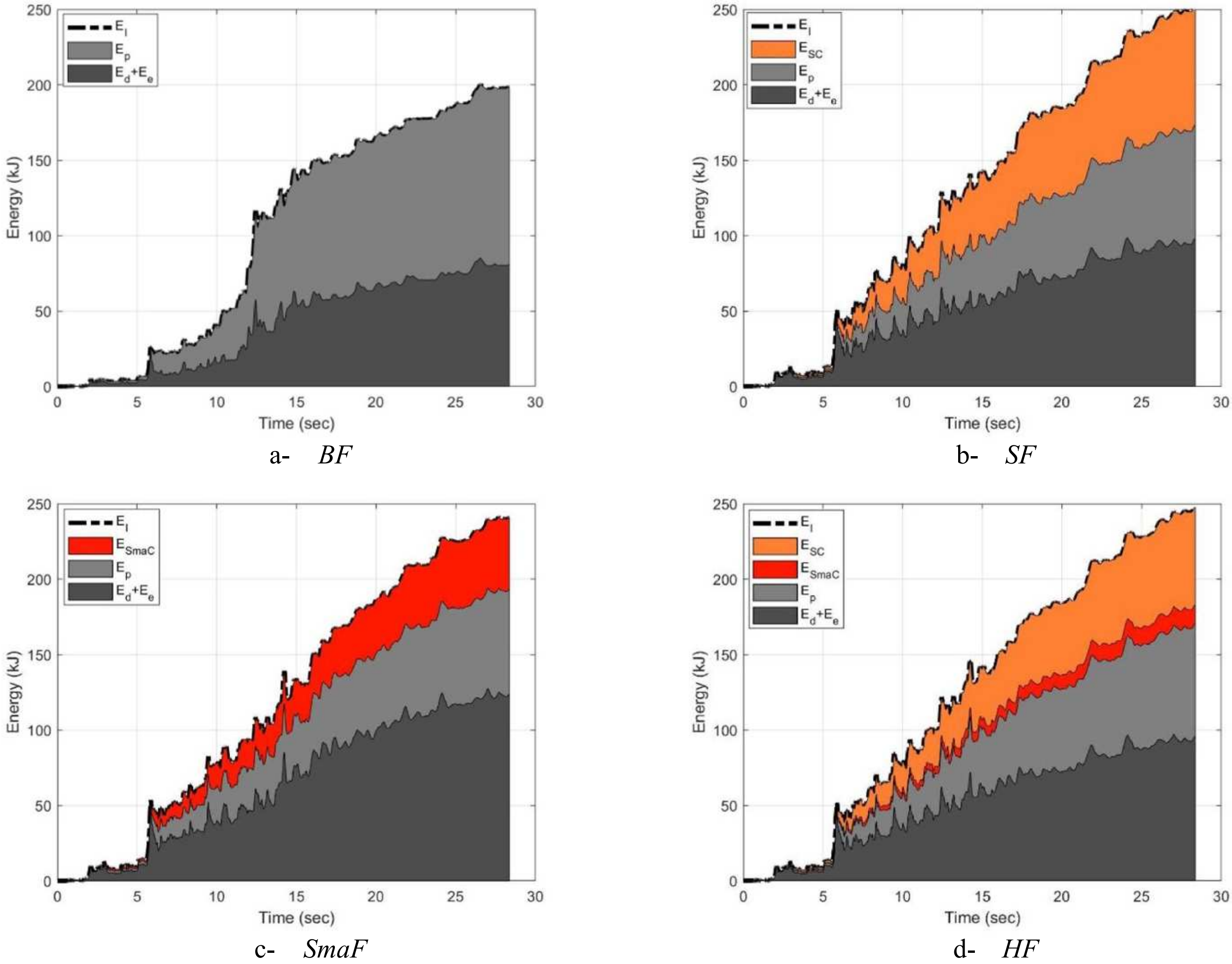

Figure 20. Seismic input energy and its distribution for the record RSN448.

equation, u is the relative displacement of a single degree of freedom system and dots stand for its time derivatives. M, C, and $F(u)$ are the mass, damping, and restoring force characteristics of the system, respectively. The terms on the left side of the equation are kinetic energy (E_k), damping energy (E_d), and strain energy (E_s), respectively. The strain energy has two parts, i.e. the elastic (E_es) and plastic/hysteretic (E_p) energies. The term on the right side of the equation stands for the total input energy (E_I). The kinetic and elastic strain energies are the elastic terms of the equation. The sum of these terms is also known as elastic energy (E_e).

$$M\int \ddot{u}\dot{u}\mathrm{d}t + C\int \dot{u}^2\mathrm{d}t + \int F(u)\dot{u}\mathrm{d}t = -M\ddot{u}_g\dot{u}\mathrm{d}t. \tag{2}$$

Seismic input and/or hysteretic energy is assumed to be a better parameter to design or evaluate building performances since it considers duration-based cumulative damage, hysteretic behavior of the structural members, and characteristics of the earthquake, soil, and structure.

In figure 20, the total seismic input energy imparted to the frames and its distribution is illustrated for the record RSN448 (Morgan Hill EQ). Based on the differences in the vibrational and damping characteristics of the frames, the imparted seismic energies also varied. While 59.34% of the total input energy was dissipated by the hysteretic behavior of the structural members of BF, the ratio reduced to 29.81%, 38.84%, and 30.22% for SF, SmaF, and HF, respectively.

The ratio of the mean dissipated plastic energy to the input energy (with $\pm$1 standard deviations) for the respective frames is given in figure 21. As expected, the two energy dissipative cushions reduce the plastic deformations of structural members significantly.

Since the SmaC is more flexible in comparison to the SC, it deforms much more easily and dissipates an important amount of seismic energy. However, for the hybrid usage of the cushions, displacement of the SmaC, i.e. energy dissipation, is restricted by the stiffness of the supplementary SC.

The peak story drift of the frame can be considered as an indicator of the extent of structural damage. Its mean value for the BF case is obtained to be 6.53%. Implementing the

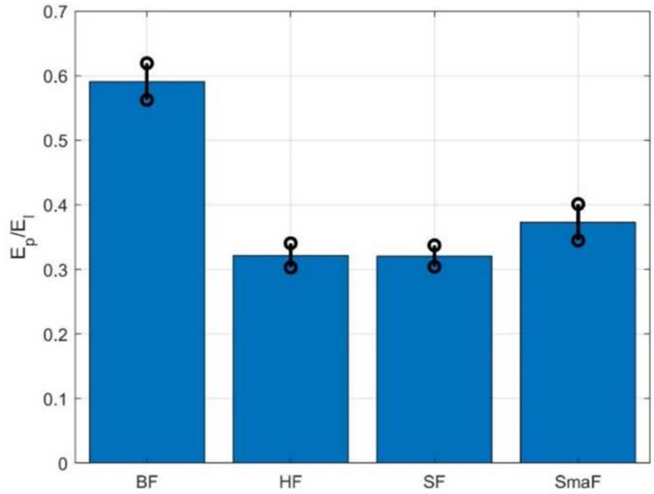

Figure 21. Dissipated energy by structural members to seismic input energy ratios.

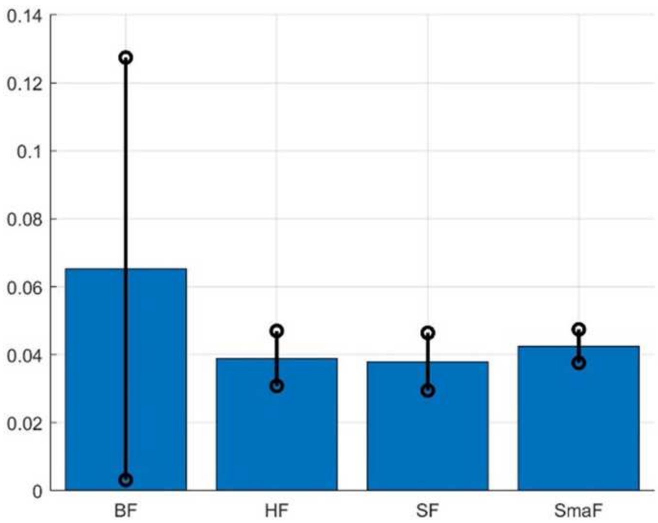

Figure 22. Obtained maximum story drifts of the frames.

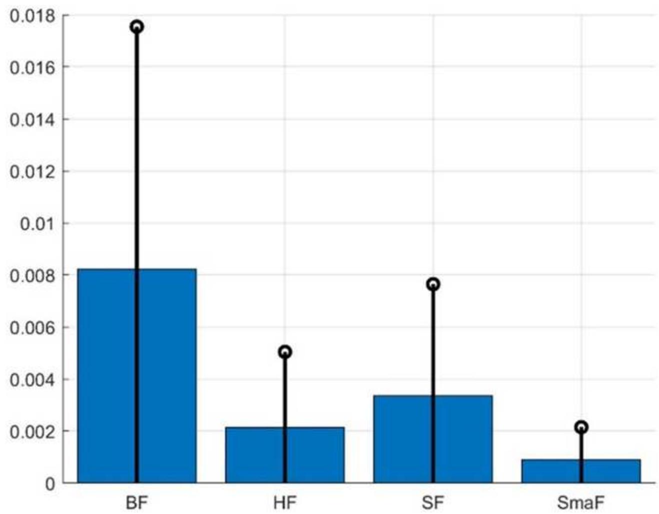

Figure 23. Obtained residual story drifts of the frames.

cushions to the bare frame reduced the maximum drifts to 3.80%, 4.25%, and 3.89% for the SF, SmaF, and HF, respectively. The mean values and standard deviations are depicted in figure 22. While the maximum drift of the bare frame disperses in a wide range, implementing the cushions to the frame reduces both the peak drift and its scattering significantly. There is a difference in the maximum drifts of SF and SmaF; the drifts obtained for the HF are similar to that of the SF.

The amount of the residual drifts is assumed as a proxy to evaluate the post-earthquake efficiency of the energy dissipative cushions, see figure 23. Residual drifts of the SmaF are almost zero (0.2% at max) while it reached up to 1.8% for the BF. Even though the SCs reduced the residual drifts at a certain level, it was not sufficient for many cases.

The damage of the frames can also be linked to the peak and residual rotations of the structural members. Mean values of the peak and residual rotations of the frame elements and their ± 1 standard deviations are plotted in figures 24(a)–(d) for the columns and the beams, respectively. Similar to the story responses, rotations of the structural members are reduced significantly by implementing the cushions.

Based on the results of the nonlinear response history analyses, it can be stated that implementing the cushions significantly improves the seismic performance of a frame.

While the SCs are quite effective to reduce the plastic energy demand of structural members and maximum displacement responses, the SmaC is favorable to reduce residual deformations and drifts. As an alternative solution, the HFs take advantage of both cushions. Its ability to reduce maximum displacements is close to that of the SF, it also has a tolerable difference in terms of the post-earthquake behavior in comparison to the SmaF. Hence, the hybrid frame might be suggested as an optimal solution to improve the seismic performance of structures; this warrants further studies in the future to optimize the hybrid cushions (in terms of material placement and cushion geometry).

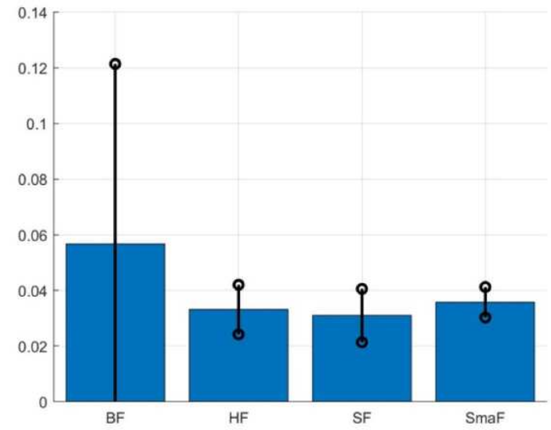

a- Maximum column rotation

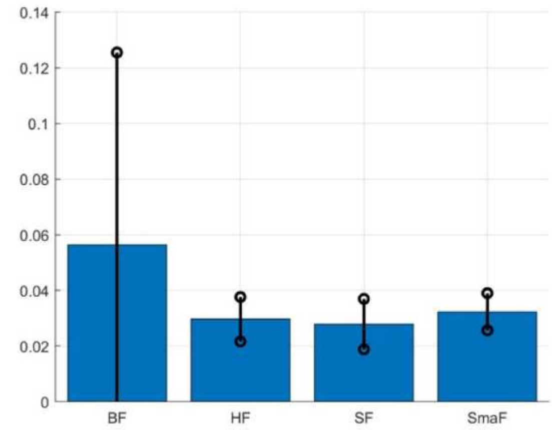

b- Maximum beam rotation

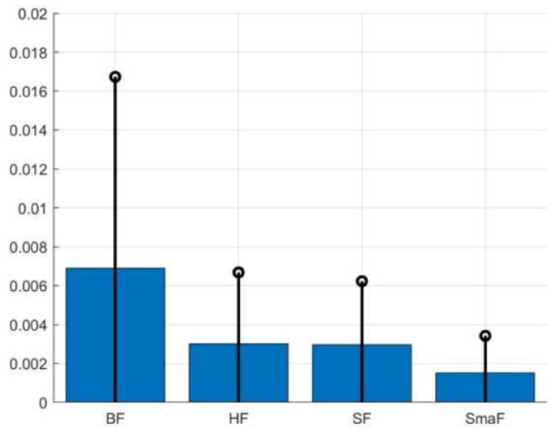

c- Residual column rotation

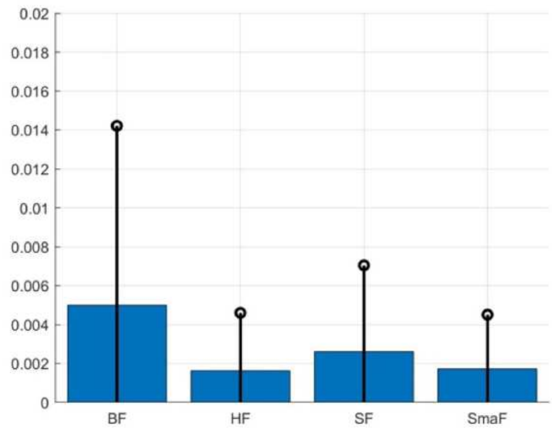

d- Residual beam rotation

Figure 24. Maximum and residual plastic rotations of structural members.

5. Conclusion

Energy dissipative SC were found to be quite efficient to dissipate seismic energy in the literature. However, its post-earthquake performance, i.e. residual drifts and deformations, was the main drawback of such cushion dampers. In this study, the base material of the energy dissipative cushions (i.e. steel) was replaced with Ni–Ti SMA to improve the post-earthquake performance of the damper (SmaC). Initially, the performance of the dampers is compared by comprehensive finite element analyses. Hereafter, steel and SMA cushions are implemented in an experimental testing frame. Seismic performance of the bare frame and the improved ones, i.e. (a) using only the SCs, (b) using only the SMA cushions, (c) using both steel and shape memory cushions (labeled here as HF) are evaluated through nonlinear response history analyses. SCs are found to be more effective to reduce peak responses while SmaCs are more favorable to reduce residual displacements and deformations. So, combining the SCs and SmaCs in a single energy dissipative system is suggested to reach optimal seismic performance for structures. The analyzed HF is promising since it can reduce peak responses and residual drifts and deformations.

The following individual conclusions might also be driven from the performed study;

- the yielding force of the SmaC is found to be slightly smaller comparing to the SC. However, its ultimate force is larger at the higher displacement levels due to the higher post-yield stiffness ratio of Ni–Ti.
- The damping ratio of the SmaC varies between 8% and 10% due to its flag shape hysteretic behavior. However, no residual displacement is achieved at the end of loading cycles.
- Implementing the SCs and SmaCs in the analyzed frames reduced the plastic energy demand of the structural members from 59.34% to 29.81% and 38.84%, respectively. In the case when the SCs and SmaCs were combined in the frame analysis, the ratio was reduced to 30.22%.

Data availability statement

The data that support the findings of this study are available upon reasonable request from the authors.

Acknowledgments

The experiments performed for the analyzed testing frame were performed by MSc Murad Safarli as a master thesis under supervision of Professor Dr Ercan Yüksel. The authors gratefully acknowledge MSc Murad Safarli, PhD candidate Furkan Çalım and Professor Dr Ercan Yüksel to share their valuable experimental data.

ORCID iDs

Ahmet Güllü https://orcid.org/0000-0001-6678-9372
Josiah Owusu Danquah https://orcid.org/0000-0002-9597-6916

References

[1] Aiken I 1996 Passive energy dissipation—hardware and applications *Proc. SEAOSC Symp. on Passive Energy Dissipation Systems for New and Existing Buildings* (*Los Angeles, CA*) http://siecorp.com/publications/papers/ida_1996a.pdf)

[2] Sadek F, Mohraz B, Taylor A W and Chung R M 1996 *Passive Energy Dissipating Devices for Seismic Applications Report No* 5923*, Building and Fire Research Laboratory* (Gaithersburg, MD: National Institute of Standards and Technology)

[3] Soong T T and Spencer Jr B F Jr 2002 Supplemental energy dissipation: state-of-the-art and state-of-the-practice *Eng. Struct.* **24** 243–59

[4] Dal Lago B, Biondini F and Toniolo G 2017 Friction-based dissipative devices for precast concrete panels *Eng. Struct.* **147** 356–71

[5] Soydan C, Yüksel E and Irtem E 2014 The behavior of a steel connection equipped with the lead extrusion damper *Adv. Struct. Eng.* **17** 25–39

[6] Soydan C, Yüksel E and Irtem E 2018 Retrofitting of pinned beam–column connections in RC precast frames using lead extrusion dampers *Bull. Earthq. Eng.* **16** 1273–92

[7] Soydan C, Yüksel E and İrtem E 2020 Seismic performance improvement of single-storey precast reinforced concrete industrial buildings in use *Soil Dyn. Earthq. Eng.* **135** 106167

[8] Zhou L, Wang X and Ye A 2019 Low cycle fatigue performance investigation on transverse steel dampers for bridges under ground motion sequences using shake-table tests *Eng. Struct.* **196** 109328

[9] Sonmez M, Aydin E and Karabork T 2013 Using an artificial bee colony algorithm for the optimal placement of viscous dampers in planar building frames *Struct. Multidiscip. Optim.* **48** 395–409

[10] Liu Y, Wang K, Mercan O, Chen H and Tan P 2020 Experimental and numerical studies on the optimal design of tuned mass dampers for vibration control of high-rise structures *Eng. Struct.* **211** 110486

[11] Safecladding Project 2015 Improved fastening systems of cladding panels for precast buildings in seismic zones

[12] Karadoğan F, Yüksel E, Khajehdehi A, Özkaynak H, Güllü A and Şenol E 2019 Cyclic behavior of reinforced concrete cladding panels connected with energy dissipative steel cushions *Eng. Struct.* **189** 423–39

[13] Colombo A, Lamperti M T, Negro P and Toniolo G 2016 *Design Guidelines for Wall Panel Connections* eds (Ispra, Italy: European Union) (https://doi.org/10.2788/546845)

[14] ISO 22502:2020 Simplified design connections of concrete claddings to concrete structures

[15] Yüksel E, Karadoğan F, Özkaynak H, Khajehdehi A, Güllü A, Smyrou E and Bal I E 2018 Behaviour of steel cushions subjected to combined actions *Bull. Earthq. Eng.* **16** 707–29

[16] Özkaynak H 2018 Earthquake behavior of steel cushion-implemented reinforced concrete frames *Earthq. Eng. Eng. Vib.* **17** 385–401

[17] Güllü A 2018 Determination of the inelastic displacement demand and response control of steel frame type structures by seismic energy equations *PhD Dissertation* Istanbul Technical University, Istanbul, Turkey

[18] Güllü A, Yüksel E and Yalçın C 2018 Seismic energy based design: numerical evaluation of diverse MDOF systems *Proc. 16th European Conf. on Earthquake Engineering* (*Thesaloniki, Grece*)

[19] Özkaynak H, Güllü A, Gökçe T, Khajehdehi A, Mahdavi M, Azizisales F, Bal I E, Smyrou E, Yüksel E and Karadoğan F 2014 Energy dissipative steel cushions *Proc. 2nd European Conf. on Earthquake Engineering and Seismology* (*Istanbul, Turkey*)

[20] Özkaynak H, Khajehdehi A, Güllü A, Azizisales F, Yüksel E and Karadoğan F 2018 Uni-axial behavior of energy dissipative steel cushions *Steel Compos. Struct.* **27** 661–74

[21] Güllü A, Smyrou E, Khajehdehi A, Özkaynak H, Bal I E, Yüksel E and Karadoğan F 2019 Numerical modelling of energy dissipative steel cushions *Int. J. Steel Struct.* **19** 1331–41

[22] Atasever K, Inanaga S, Tekeuchi T, Terazawa Y and Çelik O C 2020 Experimental and numerical studies on buckling restrained braces with posttensioned carbon fiber composite cables *Earthq. Eng. Struct. Dyn.* **49** 1640–61

[23] Nobahar E, Asgarian B, Mercan O and Soroushian S 2020 A post-tensioned self-centering yielding brace system: development and preformance-based seismic analysis *Struct. Infrastruct. Eng.* **17** 392–412

[24] Shi F, Özbulut O E and Zhou Y 2019 Influence of shape memory alloy brace design parameters on seismic performance of self-centering steel frame building *Struct. Control Health Monit.* **27** e2462

[25] Wang B, Zhu S and Casciati F 2020 Experimental study on novel self-centering seismic base isolators incorporating superelastic shape memory alloys *J. Struct. Eng.* **146** 04020129

[26] Song G, Ma N and Li H-N 2006 Applications of shape memory alloys in civil structures *Eng. Struct.* **28** 1266–74

[27] Wang W, Fang C, Zhang A and Liu X 2019 Manufacturing and performance of a novel self-centering damper with shape memory alloy ring springs for seismic resilience *Struct. Control Health Monit.* **26** e2337

[28] Sharabash A M and Andrawes B O 2009 Application of shape memory alloy dampers in the seismic control of cable-stayed bridges *Eng. Struct.* **31** 607–16

[29] Zareie S, Mirzai N, Alam M S and Seethaler R J 2017 An introduction and modeling of novel shape memory alloy-based bracing *Proc. CSCE2017* (*Vancouver, Canada*)

[30] Moradi S and Alam M S 2015 Feasibility study of utilizing superelastic shape memory alloy plates in steel beam–column connections for improved seismic performance *J. Intell. Mater. Syst. Struct.* **26** 463–75

[31] Fang C, Wang W, He C and Chen Y 2017 Self-centering behaviour of steel and steel-concrete composite connections equipped with NiTi SMA bolts *Eng. Struct.* **150** 390–408

[32] Hu J W 2016 Seismic analysis and parametric study of SDOF lead-rubber bearing (LRB) isolation systems with recentering shape memory alloy (SMA) bending bars *J. Mech. Sci. Technol.* **30** 2987–99

[33] Zuo X-B, Li A-Q, Sun W and Sun X-H 2009 Optimal design of shape memory alloy damper forcable vibration control *J. Vib. Control* **15** 897–921
[34] Zhang Y, Hu X and Zhu S 2009 Seismic performance of benchmark base-isolated bridges with superelastic Cu–Al–Be restraining damping device *Struct. Control Health Monit.* **16** 668–85
[35] Dilibal S, Şehitoglu H, Hamilton R F, Maier H J and Chumlyakov Y 2011 On the volume change in Co–Ni–Al during pseudoelasticity *Mater. Sci. Eng.* A **528** 2875–81
[36] Hamilton R F, Dilibal S, Şehitoglu H and Maier H J 2011 Underlying mechanism of dual hysteresis in NiMnGa single crystals *Mater. Sci. Eng.* A **528** 1877–81
[37] Saleeb A, Dhakal B, Dilibal S, Owusu-Danquah J and Padula I I S 2015 On the modeling of the thermo-mechanical responses of four different classes of NiTi-based shape memory materials using a general multi-mechanism framework *Mech. Mater.* **80** 67–86
[38] Dilibal S 2016 The effect of long-term heat treatment on the thermomechanical behavior of NiTi shape memory alloys in defense and aerospace applications *Def. Sci. J.* **15** 1–23
[39] Dilibal S, Hamilton R F and Lanba A 2017 The effect of employed loading mode on the mechanical cyclic stabilization of NiTi shape memory alloys *Intermetallics* **89** 1–9
[40] Dilibal S 2018 Stabilized actuation of a novel NiTi shape memory alloy actuated flexible structure under thermal loading *Mater. Tehnol.* **52** 599–605
[41] Cortés-Puentes W L and Palermo D 2017 SMA tension brace for retrofitting concrete shear walls *Eng. Struct.* **140** 177–88
[42] Zareiea S, Salem R I, Seethalerc J and Zabihollah A 2020 Recent advances in the applications of shape memory alloys in civil infrastructures: a review *Structures* **27** 1535–50
[43] Bruno S and Valente C 2002 Comparative response analysis of conventional and innovative seismic protection strategies *Earthq. Eng. Struct. Dyn.* **31** 1067–92
[44] Baratta A and Corbi O 2002 On the dynamic behaviour of elastic-plastic structures equipped with pseudoelastic SMA reinforcements *Comput. Mater. Sci.* **25** 1–13
[45] DesRoches R and Delemont M 2002 Seismic retrofit of simply supported bridges using shape memory alloys *Eng. Struct.* **24** 325–32
[46] Shi F, Saygılı G, Özbulut O E and Zhou Y 2020 Risk-based mainshock-aftershock performance assessment of SMA braced steel frames *Eng. Struct.* **212** 110506
[47] Cao S, Özbulut O E, Wu S, Sun Z and Deng J 2020 Multi-level SMA/lead rubber bearing isolation system for seismic protection of bridges *Smart Mater. Struct.* **29** 055045
[48] Cao S and Özbulut O E 2020 Long-stroke shape memory alloy restrainers for seismic protection of bridges *Smart Mater. Struct.* **29** 115005
[49] Zhang R, Jiang J, Jia Y and Wang C 2021 Influence of mechanical layout of shape memory alloy damping inerter (SDI) for vibration control *Smart Mater. Struct.* **30** 085021
[50] Altuğ-Peduk G, Dilibal S, Harrysson O and Özbek S 2021 Experimental investigation on the EBM-based additively manufactured prismatic nickel–titanium SMA components *Russ. J. Nonferr. Met.* **62** 357–67
[51] Dilibal S, Nohut S, Kurtoğlu C and Owusu-Danquah J 2021 Data-driven generative design integrated with hybrid additive subtractive manufacturing (HASM) for smart cities *Advanced Sciences and Technologies for Security Applications* ed C Chakraborty, J C W Lin and M Alazab (Berlin: Springer) 205–28
[52] Wang W, Fang C and Liu J 2016 Large size superelastic SMA bars: heat treatment strategy, mechanical property and seismic application *Smart Mater. Struct.* **25** 075001
[53] Saleeb A F, Padula I I S A and Kumar A 2011 A multi-axial, multimechanism based constitutive model for the comprehensive representation of the evolutionary response of SMAs under general thermomechanical loading conditions *Int. J. Plast.* **27** 655–87
[54] Owusu-Danquah J S, Saleeb A F and Soudah M A 2021 Cyclic pseudoelastic training and two-way shape memory behavior of a NiTi alloy with small irrecoverable plastic strains: numerical modeling *Int. J. Solids Struct.* **217–218** 178–92
[55] Owusu-Danquah J S, Saleeb A F, Dhakal B and Padula S A 2015 A comparative study of $Ni_{49.9}Ti_{50.1}$ and $Ni_{50.3}Ti_{29.7}Hf_{20}$ tube actuators *J. Mater. Eng. Perform.* **24** 1726–40
[56] Owusu-Danquah J S and Saleeb A F 2017 On the cyclic stability of the thermomechanical behavior of NiTi shape memory cylindrical actuators *Eur. J. Mech.* A **64** 143–59
[57] Ikeda T, Nae F A, Naito H and Matsuzaki Y 2004 Constitutive model of shape memory alloys for unidirectional loading considering inner hysteresis loops *Smart Mater. Struct.* **13** 916
[58] Qiu C, Fang C, Liang D, Du X and Yam M C 2020 Behavior and application of self-centering dampers equipped with buckling-restrained SMA bars *Smart Mater. Struct.* **29** 035009
[59] Güllü A, Körpeoğlu S G and Selek Kılıçarslan E S 2021 Multi-objective optimal sizing of energy dissipative steel cushions for longitudinal loading *Struct. Multidiscip. Optim.* **63** 2955–67
[60] Güllü A, Yüksel E, Yalçın C, Dindar A A, Özkaynak H and Büyüköztürk O 2019 An improved input energy spectrum verified by the shake table tests *Earthq. Eng. Struct. Dyn.* **48** 27–45
[61] Owusu-Danquah J S and Saleeb A F 2017 On the modeling of the effect of processing and heat treatment on actuation behaviors of high temperature ternary and quaternary shape memory alloys *J. Alloys Compd.* **714** 493–501
[62] Chopra A K 1995 *Dynamics of Structures: Theory and Applications to Earthquake Engineering* (Englewood Cliffs, NJ: Prentice-Hall)
[63] Shi F, Zhou Y, Özbulut O E and Cao S 2021 Development and experimental validation of anchorage systems for shape memory alloy cables *Eng. Struct.* **228** 111611
[64] CSI SAP 2000 Structural analysis software
[65] Safarli M 2020 An experimental study to determine the effect of lap splice location in columns on the behaviour of rc frame type systems master *Thesis Dissertation* Istanbul Technical University Istanbul Turkey, Turkish
[66] Şenol E, Dindar A A, Yüksel E and Karadoğan F 2015 Energy dissipation characteristics of slab type buildings with special connectors *Proc. 5th Int. Conf. on Computational Methods in Structural Dynamics and Earthquake Engineering Methods in Structural Dynamics and Earthquake Engineering Crete Island* (*Greece*) (https://doi.org/10.4274/tjh.2014.0277)
[67] Andrawes B and DesRoches R 2005 Unseating prevention for multiple frame bridges using superelastic devices *Smart Mater. Struct.* **14** S60–7
[68] ACI 374.2R-13 Guide for testing reinforced concrete structural elements under slowly applied simulated seismic loads, ACI
[69] Pacific Earthquake Engineering Research Center *Ground Motion Database NGA-West2* (http://ngawest2.berkeley.edu/)
[70] Al Atik L and Abrahamson N 2010 An improved method for nonstationary spectral matching *Earthq. Spectra* **26** 601–17
[71] Turkish Building Earthquake Code 2018 *Specifications for Buildings to be Built in Seismic Areas Ministry of Public Works and Housing* (Ankara, Turkey)
[72] Akiyama H 1985 *Earthquake-Resistant Limit-State Design for Buildings* (Tokyo, Japan: University of Tokyo)